DOI: https://doi.org/10.54966/jreen.v28i1.1342

Journal of Renewable Energies

Revue des Energies Renouvelables

journal home page: https://revue.cder.dz/index.php/rer

Conference paper

Biological properties study of bioactive diopside prepared from local raw materials

Souheila Zouai [a,*], **Asma Fares** [a], **Salma Khuwaylid** [a], **Khawla Ezzedine** [a], **Abdelhamid Harabi** [b]

[a] *Laboratoire de Physique Appliquée et Théorique, Université Larbi-Tébessi, 12000 Tébessa, Algeria*

[b] *Department of Physics, Constantine University 1, 25000 Constantine, Algeria*

ARTICLE INFO

Article history:

Received January 11, 2024

Accepted January 29, 2025

Keywords:

Diopside,
Ultrafine Structures,
Simulated body fluid,
Carbonate- hydroxyapatite,
Granule size.

ABSTRACT

In this study, it was synthesized of ultrafine-structured diopside granules using the sintering method from solid raw materials (Dolomite) at a temperature of 1300 °C for 2 hours. Following the preparation, the powders were homogenized within the [200-400 µm] range and then immersed in simulated body fluid (SBF) at 37°C for 2, 7, 14, and 21 days. Following different soaking durations, the samples were carefully extracted from the fluids using deionized water. Subsequently, they were air-dried at room temperature prior to examining the impact of immersion on their crystalline properties. This involved monitoring the variation in ion concentration and pH during the immersion periods, as well as using X-ray diffraction (XRD), characterization through scanning electron microscopy (SEM), Fourier transform infrared (FTIR), *and Inductively Coupled Plasma-Optical Emission Spectroscopy (ICP-OES) analysis*. The findings revealed the partial dissolution of ultrafine Structured diopside granules and the development of a layer of carbonate-hydroxyapatite ($Ca_{10.00}P_{6.00}O_{26.14}H_{2.60}C_{0.02}$) on the surface of the samples after seven days of immersion, with a granular size estimated at D_{nm}=102.96 nm. This volume continued to increase with longer dipping durations, reaching D_{nm}=205.94 nm for samples immersed for 21 days. Finally, the results obtained suggest that ultrafine-structured diopside granules are promising candidates for bone regeneration.

1. INTRODUCTION

Significant advancements have been achieved in bone tissue engineering over the last two decades. The emergence of implantable ceramic scaffolds, which facilitate the growth of bone tissue, offers new possibilities for treating previously untreatable large bone defects resulting from tumors, trauma, and

* *Corresponding author, E-mail address: souheila@univ-tebessa.dz*
Tel : + 213 655244478

ISSN: 1112-2242 / EISSN: 2716-8247

congenital issues (Venkatraman et al., 2020). Polycrystalline silicate ceramics, particularly diopside, have garnered attention for their bioactivity and ability to form chemical interactions with the surrounding bone, leading to the formation of a biological apatite layer (Shen et al., 2020; Zhu et al., 2020). Research has showcased the exceptional bioactivity of calcium-silicate ceramics like wollastonite (Liu et al., 2004) and diopside (Collin et al., 2021). These materials exhibit diverse functionality and favorable mechanical properties, making them well-suited for bone tissue engineering (Palakurthy et al., 2021; Nonami et al.,1990; Kazemi et al., 2017). Notably, diopside stands out for its impressive fracture toughness, mechanical strength surpassing the mechanical properties of bone, slow degradation, enhanced hydroxyapatite (HA) deposition, and in vivo biocompatibility (Wu & Chang, 2007; Nonami et al.,1992; Vallet-Regi et al., 1999). Recently, bioactive diopside ultrafine Structures ($CaMgSi_2O_6$) have emerged as promising materials for bone replacement and as nanocarriers for drug delivery. The structural properties of this ceramic play a crucial role in its ability to bond with bone tissue. Understanding the correlation between structure and biological function is essential for achieving optimal clinical results (Sobhani et al., 2023).

Solid-state reactions have conventionally been employed in the synthesis of diopside powder (Titorenkova et al., 2022). However, generating ultrafine-structured diopside granules using this method presents challenges due to the high temperatures and prolonged reaction time, leading to grain growth. Nevertheless, this approach remains valuable for large-scale production. Ultrafine -powders are increasingly drawing attention for their applications in medicine, electronics, and other fields. Low-temperature synthesis of diopside has been pursued through chemical methods such as hydrothermal (Python et al., 2007), sol-gel (Yamamoto et al., 2019), and precipitation (Iwata et al., 2004), as well as the utilization of natural waste materials like rice husk ash and eggshells (Palakurthy et al., 2021). Venkatraman et al. (Venkatraman et al., 2022). successfully produced monticellite and diopside from bio-waste using a self-propagating auto-combustion technique and observed the influence of formation temperature on grain size. Another study incorporated various diopside concentrations into forsterite to create porous scaffolds, reducing the sintering temperature and enhancing bioactivity and biodegradability with 10 wt% diopside (Sadeghzade et al., 2017). Nevertheless, due to the complex nature of the sample preparation, an alternative method has been proposed, focusing on substituting expensive materials with more readily available and cost-effective raw materials found abundantly worldwide. Several studies have explored the use of these indigenous raw materials in bioceramic applications (Mezahi et al., 2009; Mezahi et al.,2012; Harabi & Chehlatt., 2013; Harabi & Zouai, 2014). Efforts have been dedicated to mitigating excessive grain growth (Harabi et al., 2011). Careful consideration of key factors in diopside production, including milling techniques, compacting pressure, sintering temperature, and holding time, can lead to the production of promising diopside-based bioceramics. A straightforward and energetically efficient approach entails using a vibratory multidirectional milling system, incorporating the bimodal distribution of highly resistant ceramics, to obtain sub-micron-sized powders. Consequently, the primary aim of this study is to comprehensively assess the bioactivity of pure ultrafine-scale diopside prepared using a solid-state synthesis method from locally sourced raw materials. This will be achieved through a thorough investigation into the formation of hydroxyapatite (HA) on the material's surface when exposed to a simulated body fluid (SBF) solution.

2. EXPERIMENTAL

2.1 Preparation of powders

ultrafine-structured diopside granules were synthesized using a solid-state reaction method. A blend of highly pure SiO_2 and doloma (CaO.MgO), sourced from local dolomite raw material ($CaCO_3$.$MgCO_3$), was heated at 900°C for 2 hours. The mixture was then treated with distilled water at 150°C for 12 hours,

and subsequently subjected to a second heating at 600°C for 2 hours. The doloma utilized boasts approximately 99.6 wt.% purity, with minimal impurities such as 0.27 wt.% Fe_2O_3, 0.07 wt.% Al_2O_3, and 0.02 wt.% Na_2O, as per Ming et al. (Ming et al., 2011). This raw material is categorized as high-purity calcium and magnesium oxides ($CaO.MgO \geq 99.0\%$). The doloma was combined with 55.5 wt.% SiO_2 and the resulting mixtures were ball-milled in aqueous media for 4 hours using a specialized milling system (Harabi et al., 2015; Harabi & Harabi, 2015). A comprehensive study detailing the key features and benefits of this modified milling system was previously published and applied to the sintering of natural hydroxyapatite (Harabi et al., 2015; Harabi & Harabi, 2015). Subsequently, the powders underwent a calcination process at 700°C for 2 hours, followed by sintering at 1300°C for 2 hours.

2.2 In vitro tests (apatite forming ability)

The sintered powders' in vitro behavior was examined through their ability to generate apatite in a simulated body fluid (SBF). Following sintering at 1300 °C for 2 hours, the powders were submerged in an SBF solution mirroring the ion concentrations of human blood plasma as per Table 1 (Cho et al., 1995). The pH of the SBF solution was stabilized at 7.4 using (hydroxymethyl)-aminomethane [$(CH_2OH)_3CNH_2$] and hydrochloric acid (HCl) according to Kokubo's protocol (Cho et al., 1995). The "In vitro" test involved immersing 10 mg powders in 10 mL of SBF at 37°C for 2, 7, 14, and 21 days respectively, without replacing the SBF during the experiment. The pH level of the SBF was monitored at regular intervals. After each soaking period, the powders were removed from the solution, washed with deionized water, and air-dried at room temperature for characterization.

2.3 Characterisations

The thermal stability and phase transformations were examined using a differential thermal analyzer (DTA) in NETZSCH, Germany. The analysis was conducted over a temperature range of 30 to 1000°C in an air atmosphere, with a heating rate of 10°C per minute. The powder's phase identification and morphology, both before and after soaking in the SBF solutions (Table 1), were analyzed using various techniques. X-ray diffraction was conducted using a BRUKER D8 ADVANCE instrument in Karlsruhe, Germany, operating with CuKα radiation (λ = 0.154 nm) and a Ni filter, at a working voltage of 40 kV and a working current of 30 mA. The crystallite size in the synthesized powders was estimated using the Scherrer equation as follows:

$$D_n = \frac{0.9 \quad \lambda}{\beta \cos\theta} \tag{1}$$

Where β is the full-width at half maximum intensity (FWHM), λ is the wavelength, Θ is Bragg's angle, and D_n is the apparent crystallite size (nm). Fourier-transform infrared spectroscopy was performed with a Bruker Equinox 55 instrument in the range of 4000-400 cm^{-1}. The surfaces of the powders were examined through Scanning Electron Microscopy using a HITACHI JSM-6301 F in Tokyo, Japan, at an accelerating voltage of 7 kV. Furthermore, the concentrations of Ca, P, and Mg ions in the SBF solution after soaking were quantified using Inductively Coupled Plasma-Optical Emission Spectroscopy with a Spectro Ciros Vision instrument in Karlsruhe, Germany.

Table 1. Ion concentration of the SBF in comparison to human blood plasma.

Types	Ion concentrations [mmol/L]							
	Na^+	K^+	Mg^{2+}	Ca^{2+}	Cl^-	HCO^{3-}	HPO_4^{2-}	SO_4^{2-}
SBF	142.5	5.0	1.5	2.5	147.8	4.2	1.0	0.5
Blood plasma	142.5	5.0	1.5	2.5	103.0	27.0	1.0	0.5

3. RESULTS AND DISCUSSIONS

3.1 Characterisation of the $CaMgSi_2O_6$ powders

In this study, we used dolomite stone sourced from Algerian sites of Batna Province, characterized by a light brown tint and labeled as D1. It has a good density (ρ = 2.69 g/cm³), representing 93.76% of the theoretical density of dolomite. The results of X-ray diffraction, shown in Fig. (1a), revealed through comparison with the ICDD File element identification cards that all diffraction lines belong to the dolomite powder D1. No impurities or other phases were detected in the extracted spectrum, demonstrating the relatively high purity of the local dolomite. The Differential Thermal Analysis (DTA) curve depicted in Fig. (1b) indicates that the temperature for diopside nucleation falls within the range of 740 to 750°C.

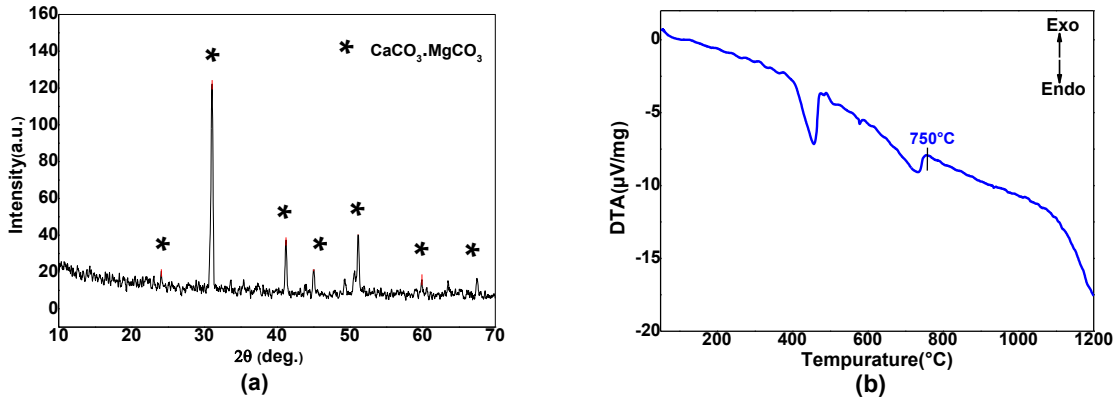

Fig 1. (a) XRD pattern of dolomite raw material and (b) DTA curve of the prepared diopside powders.

The XRD powder data underwent quantitative X'Pert High Score refinement analysis using a new software module introduced by Philips Analytical. This module, known as X'Pert High Score, is specifically tailored to simplify and enhance the reliability of phase identification for complex phase mixtures. It integrates various robust analytical tools into a user-friendly program compatible with Windows, aiming to streamline the analysis process.

The XRD patterns in Fig. (2) depict the diopside powders sintered at 1300 °C for 2 hours before immersion in the SBF solution. The XRD spectrum displayed prominent diffraction peaks at the 2Ɵ angle regions with intensities of 26.510, 27.452, 29.713, 30.185, 30.771, 34.763, 35.536, 39.007, 42.141, 42.715, 44.092, 45.054, 49.494, 49.7381, 51.787, 56.417, and 65.352. These correspond to the crystal planes represented by the Miller indices (021), (220), (-220), (310), (-311), (-131), (-112), (311), (-331), (-421), (041), (202), (510), (-512), (-531), and (531). The observed peaks matched the ICDD File No. 01-072-1497. The diopside crystallite structure was determined to be monoclinic, with lattice constant parameters a = 9.776, b = 8.979, c = 5.267 Å, and β = 105.94°. Analysis of the XRD spectrum reveals a typical pattern for diopside powders produced through a simple and efficient vibratory multidirectional milling system. The combined effects of vibration and rotation improve dispersion by inducing intense collisions, which subsequently reduce particle size. The XRD analysis confirms that the initial calcined powder is indeed diopside, with a chemical composition of $CaMgSi_2O_6$. Moreover, the spectrum indicates that all peaks are exclusive to the diopside structure, with no additional impurity peaks detected. The crystallite size was calculated using the Debye-Scherer equation (see Eq. (1)) based on the full width at half maximum value in the XRD pattern, resulting in a size of approximately 660 nm, determined from the intense diffraction peak at 2θ = 29.713. This value is slightly higher than those of diopside prepared using other usual techniques (440 nm) (Palakurthy et al., 2021). Based on the information provided, ultrafine-structured diopside granules can be readily synthesized using the

sintering method from solid raw materials at relatively high temperatures, without the need for acidic catalysts.

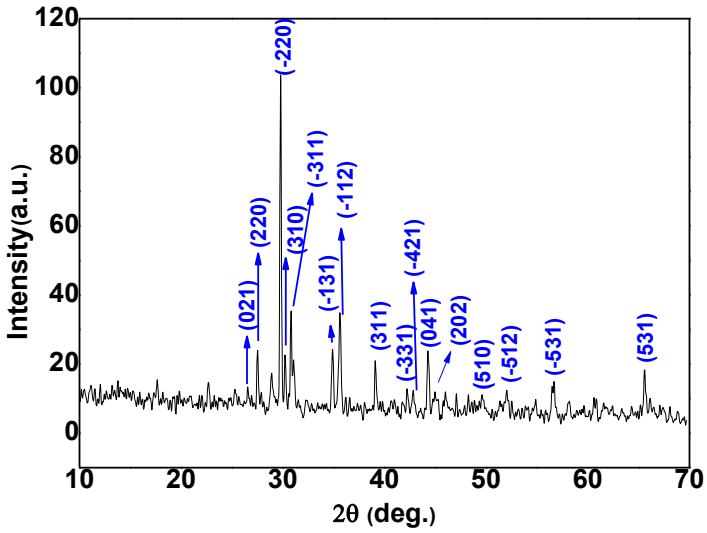

Fig 2. XRD pattern of the $CaMgSi_2O_6$ powders sintered at 1300 °C before soaking in the SBF solution.

FTIR spectroscopy was used to determine the presence of functional groups associated with diopside. Analysis of the FTIR spectra revealed the presence of all characteristic functional groups, signifying the successful phase formation of diopside (Fig. (3a)). Upon calcination of the diopside precursor at 1300 °C, various vibrational modes were observed. These included the non-bridging bending modes of O–Mg–O bonds within the range of 457 cm^{-1} to 516 cm^{-1}. Additionally, the O–Si–O bending mode manifested as sharp dual peaks at 633 cm^{-1} and 670 cm^{-1}, while the Si–O symmetric stretching appeared as peaks ranging from 854 cm^{-1} to 967 cm^{-1}. Notably, an intense peak at 1069 cm^{-1} corresponded to the symmetric stretching of the Si–O–Si functional group. These findings indicated that diopside derived from the local raw materials ($CaCO_3.MgCO_3$) using a solid-state reaction a similar pattern of functional groups as previously reported (Omori et al., 1971).

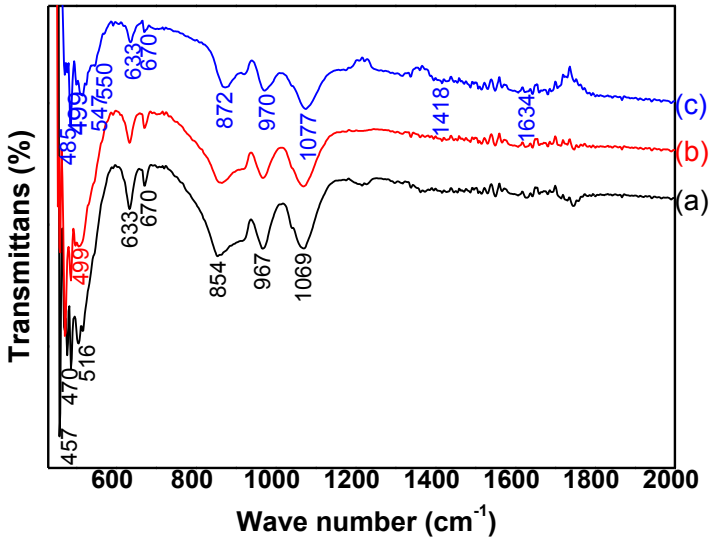

Fig 3. FTIR spectra of diopside powders (a) before, (b) after 2 days, and (c) after 21 days of immersion in SBF.

3.2 Apatite-formation ability of the $CaMgSi_2O_6$ powders

When assessing bioactivity, it is essential to consider variables such as porosity and crystallinity, as higher levels of these factors typically indicate greater bioactivity. Consequently, the bioactivity of the diopside powders was examined at a temperature of 1300 °C, which is known to produce highly crystalline powders. Validating the bioactivity of these ultrafine-structured diopside granules has the potential to unlock a wide range of applications for it.

The X-ray diffraction (XRD) patterns, depicted in Fig. (4), were analyzed to investigate the surface crystallinity of ultrafine-structured diopside granules when immersed in simulated body fluid (SBF) for different durations of 2, 7, 14, and 21 days to evaluate the hydroxyapatite deposition. After a 2-day immersion, no significant new crystalline phase was observed in the XRD analysis of diopside ceramics in SBF. However, the intensity of the diopside's crystalline peaks decreased over time, indicating its initial dissolution, subsequently enabling the precipitation of hydroxyapatite. Following 7 days of immersion, some small peaks at 2θ = 31.69 (211) and 25.87 (002) corresponding to a secondary phase emerged, consistent with the characteristics of Carbonated hydroxyapatite (CHA) ($Ca_{10.00}P_{6.00}O_{26.14}H_{2.60}C_{0.02}$) as reported in JCPDS file No. 96-900-3554. After 14 days of immersion, an additional peak of Carbonated hydroxyapatite at 2θ = 49.43 (123) appeared as minor phases. Following 21 days of immersion, there was a rise in the intensity of XRD peaks associated with Carbonated hydroxyapatite, and the distinctive peaks of CHA at 2θ = 50.35 (213) emerged after this period. However, the diopside phase continued to be predominant.

In Table 2, the interplanar d-spacings and positions (2θ) of the diffraction peaks corresponding to the X-ray patterns of the powders after 21 days of storage in SBF are presented. The calculated d-spacings closely matched the data from ICDD card 01-071-1494 for diopside and file No. 96-900-3554 for CHA. These results suggest that ultrafine-scale diopside, sourced from local raw materials, holds promise for converting into hydroxyapatite during the initial stages of soaking, aligning with previous literature reports (Wu & Chang, 2007; Choudhary et al., 2016; Iwata et al., 2004). The Debye-Scherer equation was used to calculate the crystallite size from full width at half maximum value in the XRD pattern, by selecting the intense diffraction peak at 2θ = 31.69. The research findings indicate that after seven days of immersion, the diopside granules partially dissolved, leading to the formation of a layer of carbonate-hydroxyapatite ($Ca_{10.00}P_{6.00}O_{26.14}H_{2.60}C_{0.02}$) on the sample surfaces, with an estimated granular size of D_{nm}=102.96 nm. Over longer immersion periods, this layer continued to grow, reaching D_{nm}=205.94 nm for samples immersed for 21 days. Therefore, this ultrafine-sized structure could offer valuable advantages for applications in bone tissue engineering, dentistry, and orthopedics, making the diopside more biocompatible (Kazemi et al., 2017).

Table 2. The position and characteristics of the main XRD peaks of the ultrafine-structured diopside granules after immersion in SBF for 21 days.

Pos. [°2Th.]	Height [cts]	FWHM Left [°2Th.]	d-spacing [Å]	Rel. Int. [%]	Tip Width	Matched by
29,8211	360,45	0,0669	2,99614	100,00	0,0803	01-071-1494
30,8591	231,37	0,1673	2,89768	64,19	0,2007	01-071-1494
31.9612	165,05	0,1338	2,82347	45,79	0,1606	96-900-3554
56,4223	114,49	0,2676	1,63085	31,76	0,3212	01-071-1494
25,8763	96,82	0,1004	3,42243	26,86	0,1204	96-900-3554

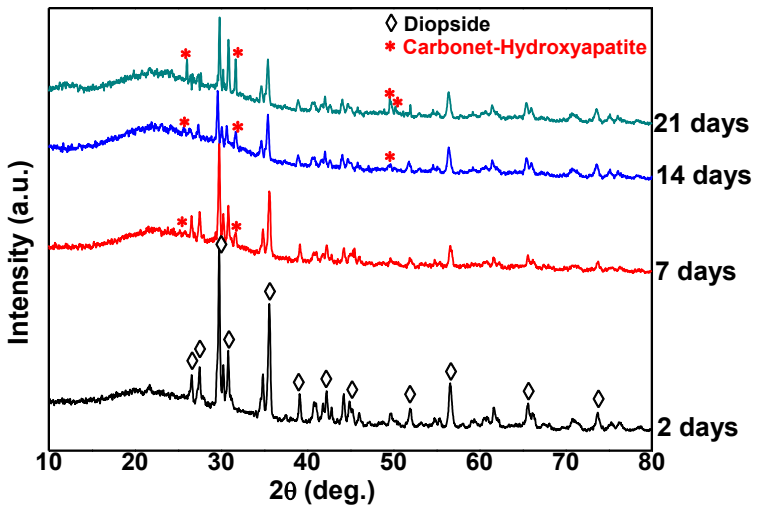

Fig 4. XRD patterns of diopside powders after immersion in SBF for 2, 7, 14, and 21 days.

Following immersion in simulated body fluid (SBF), the diopside powder surface underwent FTIR spectroscopy analysis to study the absorption bands of various functional groups and confirm the formation of carbonated hydroxyapatite. After 2 days in the SBF solution, the intensity of the silicate absorption bands decreased, indicating early-stage hydrolysis of metal ions. Furthermore, the FTIR spectra (curve b in Fig. (3)) of diopside after 2 days in SBF revealed a sharp peak of phosphate at 499 cm^{-1} (Choudhary et al., 2016). The presence of phosphate peak was evidence of the growth of hydroxyapatite on the surface of diopside after 2 days only in SBF supporting the understanding of the chemical changes occurring during the experiment. Fig. (3c) depicts the FTIR spectra of hydroxyapatite formation on the diopside surface 21 days after immersion in SBF. The analysis showed that peak intensities at ~633 and ~670 cm^{-1} related to the silicates' bending mode reduced, while peaks at ~470 and ~516 cm^{-1} corresponding to O-Mg-O were replaced with phosphate bending vibration modes at ~485 and 547 cm^{-1} (Palakurthy et al., 2021). This indicates the hydrolysis of the calcium and magnesium metal ions during the initial stages of SBF immersion. The observed phosphate peaks confirmed the mineralization of hydroxyapatite on the sample's surface. The bending vibration of the phosphate group was observed at 550 cm^{-1} (Kontonasaki et al., 2002), while the stretching vibration was noted at 972 (Choudhary et al., 2016) and 1077 cm^{-1}(Arai & Sparks, 2001). Additionally, the characteristic peak at 872 cm^{-1} corresponded to the stretching vibration of the HPO_4^{2-} group (Batool et al., 2023), providing evidence of hydroxyapatite growth on the diopside surface after SBF soaking. Moreover, the presence of a peak at ~1418 cm^{-1} indicated the presence of the carbonate functional group, suggesting the formation of a carbonated hydroxyapatite (CHA) layer on the sample surface (Barralet et al., 1998). Lastly, the band at ~1635 cm^{-1} demonstrated the bending vibrational mode of absorbed H_2O (Choudhary et al., 2019).

Figure (5a) illustrates the variations in calcium (Ca), phosphorus (P), and magnesium (Mg) concentrations in the simulated body fluid (SBF) solutions. Utilizing Inductively Coupled Plasma (ICP), the measurements revealed notable changes in the ion concentrations of the SBF solutions across different soaking durations. Specifically, the concentration of Ca and Mg in the SBF increased as the soaking time extended up to 2 days, followed by a decrease in Ca concentration. Conversely, the P concentration in the SBF solutions decreased consistently throughout the soaking periods. The rise in calcium and magnesium concentrations was attributed to the dissolution of these ions from the $CaMgSi_2O_6$ powders. In contrast, the decrease in calcium ions after 2 days of soaking was explained by the rapid consumption of Ca ions during the subsequent formation of Carbonated Hydroxyapatite $Ca_{10.00}P_{6.00}O_{26.14}H_{2.60}C_{0.02}$ on the powder surface. The reduction in phosphorus concentration was linked

to the formation of amorphous calcium phosphate and crystalline apatite on the powder surface, which absorbed P ions from the SBF solutions. The ICP measurements indicate that the increase in Ca concentration and the decrease in P concentration were caused by the formation of apatite on the surface of the $CaMgSi_2O_6$ powders during soaking in the SBF solution. Additionally, it was observed that the concentration of calcium ions during the reaction ranged from 84 to 100 ppm, falling within the reported suitable range of [80-200 ppm] for bone cell proliferation and differentiation, significantly lower than the critical value of cellular toxicity observed at 400 ppm (Yoshizawa et al., 2014; Nabiyouni et al., 2018). Furthermore, the concentration of magnesium ions during this reaction was found to be within the range of 36 to 41 ppm, significantly lower than the toxic concentration estimated at 486 ppm for the cells (Maeno et al., 2005).

The pH variation in the simulated body fluid (SBF) resulting from the immersion of diopside pellets is linked to the creation and breakdown of apatite. Initially, the pH of the fresh SBF was 7.4, but it rose to around 8 after 2 days of immersion. Subsequently, there was a noticeable decrease in pH over the remaining 19-day monitoring period (Fig. (5b)). Two factors contribute to the pH changes in SBF: firstly, ions leach from bioceramics into the physiological fluid, as diopside releases Ca^{2+} and Mg^{2+} ions from its surface into the SBF, leading to an increase in SBF pH. It is concluded that the dissolution of Ca^{2+} and Mg^{2+} ions from the sintered body during early immersion produces a silica-rich layer that promotes apatite nucleation. Additionally, as diopside grains dissolve, a porous surface layer forms, eventually being coated with nano globules of crystal aggregates of Carbonated Hydroxyapatite $Ca_{10.00}P_{6.00}O_{26.14}H_{2.60}C_{0.02}$. The subsequent pH decrease is attributed to the dominance of CHA formation, as confirmed by XRD and FTIR analyses, consuming OH^- in the SBF. Nevertheless, the results indicate a pH range of 7.4–8 when diopside specimens are immersed in SBF, closely aligning with existing literature on pH and indicating a favorable environment for in vivo bone cell culture (Shahrouzifara et al., 2019).

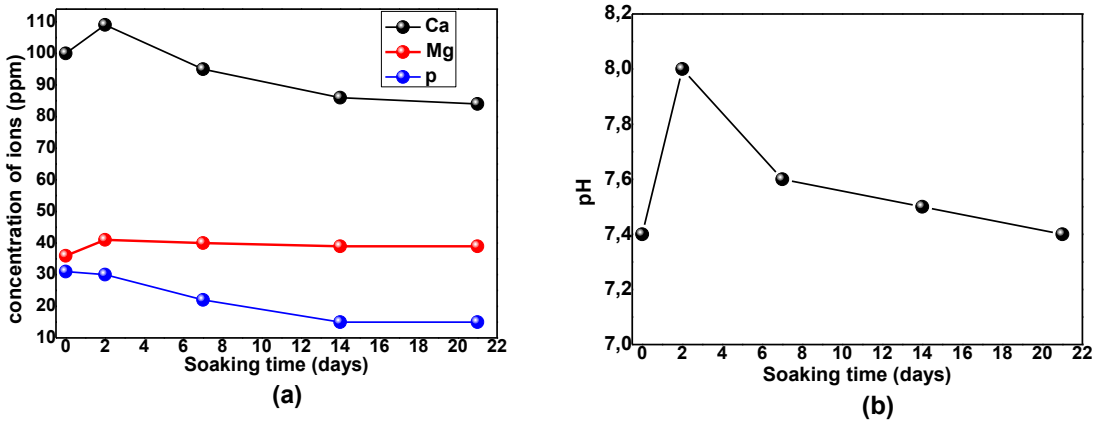

Fig 5. The Changes in: (a) Ca, Mg, and P concentrations and (b) pH of the SBF solutions after soaking the diopside powders for various periods.

Figure (6) presents the surface morphology of ultrafine-structured diopside granules before and after immersion in the SBF solution for 2 and 21 days. A comparison with the particles prior to immersion (Fig. (6a)) reveals the emergence of small ball-like particles on the diopside powders' surface after 2 days of soaking (Fig. (6b)). This surface is interspersed with numerous pores, accounting for up to 7.41% of the area. The analysis depicted in MEB Fig. (6b) indicates a maximum pore size of approximately 5 µm. Such a porous structure is advantageous as it enhances bioactivity and facilitates the release of ionic products (Jones & Hench, 2003). Additionally, microspores smaller than 10 µm are essential for promoting capillary ingrowth and cell-matrix interactions (Esfahani et al., 2008). After 21 days of

soaking, the micropores were no longer present as carbonated hydroxyapatite crystals were deposited, as shown in Fig. (6c). Initially, there is an exchange process between Ca^{2+} and Mg^{2+} ions on the diopside surface with hydrogen ions (H^+ or H_3O^+) in SBF, resulting in a decrease in calcium and magnesium content on the surface and a change in surface charge. This surface charge plays a significant role in the formation of the CHA layer on the submerged surface. Subsequently, a silica-rich layer forms on the surface due to the re-polymerization of silanol groups. These silica-rich layers attract Ca^{2+} and PO_4^{3-} ions, leading to the formation of $CaO–P_2O_5$ films. Over time, the accumulation of these ions leads to the formation of a calcium phosphate layer on the soaked surface (Saravanan & Sasikumar, 2012; Karamian et al., 2016).

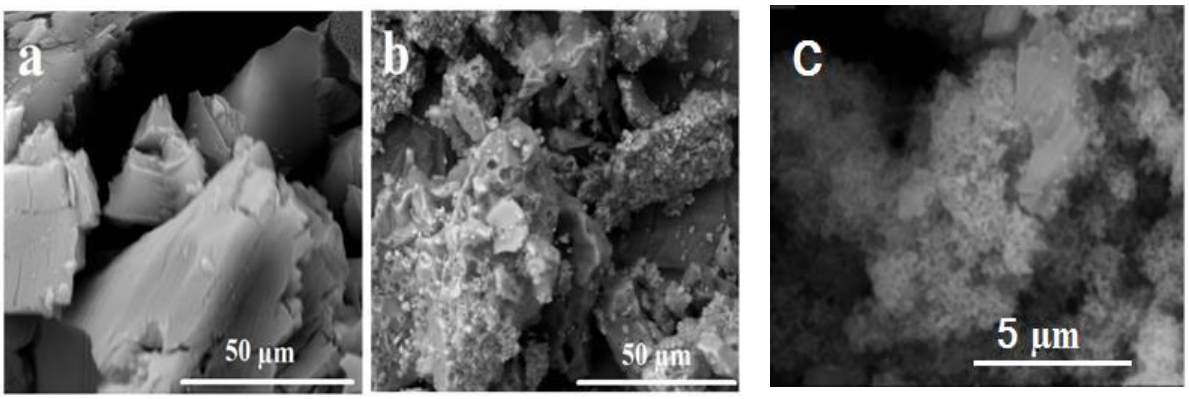

Fig 6. SEM images of the obtained diopside powders sintered at 1300 °C for 2 hours: (a) before, (b) after 2 days, and (c) after 21 days of immersion in SBF.

4. CONCLUSIONS

Numerous studies have tackled the preparation of diopside and other bioglasses, but only a few have delved into sintering ultrafine-structured diopside granules using the Solid-state reactions method and examining their bioactivity. In this study, a simple and eco-friendly one-pot Solid-state reactions method was employed to successfully produce ultrafine-structured diopside granules. This method offers several advantages, such as using cost-effective raw materials, gentle reaction conditions, a short reaction time, and a straightforward work-up process with minimal environmental impact.

The crystallization of the dried powder and the bioactivity of the sintered ultrafine-structured diopside granules were assessed by immersing it in simulated body fluid (SBF) and studying the effect of thermal treatment. The results showed that the pure ultrafine-structured diopside granules, obtained from local raw materials (Dolomite: $CaCO_3.MgCO_3$), exhibited increased reactivity in the SBF solution, demonstrating strong hydration upon immersion, which promoted the formation of hydroxyapatite on the powder surface. Furthermore, CHA formation was observed after 2 days only of immersion in the SBF solution. With longer soaking periods (7, 14, and 21 days), a dense and continuous layer of carbonate hydroxyapatite ($Ca_{10.00}P_{6.00}O_{26.14}H_{2.60}C_{0.02}$) formed on the powder surfaces, with an estimated granular size of D_{nm}=205.94 nm. As a result, $CaMgSi_2O_6$ ultrafine particles display promising bioactivity and have the potential to rapidly induce hydroxyapatite formation after immersion in SBF, making them feasible candidates for bone repair biomaterials.

NOMENCLATURE

D_n	Mean grain size [nm]
β	Stands for full width at half maximum of the peak
λ	Diffraction wavelength (0.154059) [nm]
θ	Diffraction angle

REFERENCES

Arai Y, Sparks DL. (2001) ATR–FTIR Spectroscopic Investigation on Phosphate Adsorption Mechanisms at the Ferrihydrite–Water Interface. J Colloid Interface Sci.2001; 241:317–326. doi.org/10.1006/jcis.2001.7773

Barralet J, Best S, Bonfield W. (1998) Carbonate substitution in precipitated hydroxyapatite: An investigation into the effects of reaction temperature and bicarbonate ion concentration. 1998 J Biomed Mater Res 1998; 41:79–86. DOI: 10.1002/(sici)1097-4636(199807)41:1<79::aid-jbm10>3.0.co;2-c

Batool S, Hussain Z, Rehman MR, Idrees MU. (2023) Effect of strontium and iron on the structural integrity and drug delivery of Whitlockite. Open Ceramics 2023; 14:1-7. DOI: 10.1016/j.oceram.2023.100347

Cho SB, Nakanishi K, Kokubo T, Soga N. (1995) Dependence of apatite formation on silica gel on its structure: effect of heat treatment. Journal of the American Ceramic Society 2005; 78:1769-74. DOI: 10.1111/j.1151-2916.1995.tb08887.x

Choudhary R, Vecstaudza J, Krishnamurithy G, Raghavendran HRB, Murali MR, Kamarul T, Sasikumar S, Locs J. (2016) In-vitro bioactivity, biocompatibility and dissolution studies of diopside prepared from biowaste by using sol-gel combustion method. Mater Sci Eng C 2016; 68:89–100. doi.org/10.1016/j.msec.2016.04.110.

Choudhary R, Venkatraman SK, Chatterjee A, Vecstaudza J, Yáñez-Gascón MJ, Pérez-Sánchez H, Locs J, Abraham J, Swamiappan S. (2019) Biomineralization, antibacterial activity and mechanical properties of biowaste derived diopside nanopowders, Adv Powder Technol 2019;30:1950–64. DOI: 10.1016/j.apt.2019.06.014

Collin MS, Venkatraman SK, Mohana S, Sumathi Sh, Drweesh EA, Elnagar MM, Mosa ES, Sasikumar S. (2021) Solution combustion synthesis of functional diopside, akermanite, and merwinite bioceramics: Excellent biomineralization, mechanical strength and antibacterial ability. Mater. Today Commun 2021; 27:102365. doi.org/10.1016/j.mtcomm.2021.102365.

Esfahani SIR, Tavangarian F, Emadi R. (2008) Nanostructured bioactive glass coating on porous hydroxyapatite scaffold for strength enhancement. Mater Lett 2008; 62:3428–30. DOI: 10.1016/j.matlet.2008.02.061

Hababi E, Harabi A, Foughali L, Chehlatt S, Zouai S, Mezahi FZ. (2015) Grain Growth in Sintered Natural Hydroxyapatite. ACTA PHYSICA POLONICA A 2015; 127:1161-3. DOI: 10.12693/APhysPolA.127.1161.

Harabi A, Belamri D, Karboua N, Mezahi FZ. (2011) Sintering of bioceramics using a modified domestic microwave oven: Natural hydroxyapatite sintering. Journal of Thermal Analysis and Calorimetry 2011; 104:283-9. DOI: 10.1007/s10973-010-1115-z.

Harabi A, Chehlatt S. (2013) Preparation process of a highly resistant wollastonite bioceramics using local raw materials: Effect of B_2O_3 additions on sintering and mechanical properties. Journal of Thermmal Analysis and Calorimetry 2013; 111:203-11. DOI: 10.1007/s10973-012-2242-5.

Harabi A, Harabi E, (2015) A modified milling system, using a bimodal distribution of highly resistant ceramics. Part1. A natural hydroxyapatite study. Mater Sci Eng C 2015; 51:206–15. https://doi.org/10.1016/j.msec.2015.03.003.

Harabi A, Zouai S. (2014) A new and economic approach to synthesize and fabricate bioactive diopside ceramics using a modified domestic microwave oven. Part 1: Study of sintering and bioactivity. International Journal of Applied Ceramic Technology 2014; 11:31-46. doi.org/10.1111/ijac.12047.

Iwata NY, Lee GH, Tokuoka Y, Kawashima N. (2004) Sintering behavior and apatite formation of diopside prepared by coprecipitation process. Colloids Surfaces B: Biointerfaces 2004;34(4):239–45. DOI: 10.1016/j.colsurfb.2004.01.007

Iwata NY, Lee GH, Tsunakawa S, Tokuoka Y, Kawashima N. (2004) Preparation of diopside with apatite-forming ability by sol-gel process using metal alkoxide and metal salts. Colloids Surfaces B Biointerfaces 2004; 33:1–6. DOI: 10.1016/j.colsurfb.2003.07.004.

Jones JR, Hench LL. (2003) Effect of surfactant concentration and composition on the structure and properties of sol-gel-derived bioactive glass foam scaffolds for tissue engineering. J Mater Sci 2003; 38:3783–90. DOI: 10.1023/A:1025988301542

Karamian E, Abdellahi M, Khandan A, Abdellah S. (2016) Introducing the fluorine doped natural hydroxyapatite-titania nanobiocomposite ceramic. J Alloys Comp 2016; 679:375–83. DOI: 10.1016/j.jallcom.2016.04.068

Kazemi A, Abdellahi M, Khajeh-Sharafabadi A, Khandan A, Ozada N. (2017) Study of in vitro bioactivity and mechanical properties of diopside nano-bioceramic synthesized by a facile method using eggshell as raw material. Mater Sci Eng C 2017; 71:604-10.doi.org/10.1016/j.msec.2016.10.044.

Kontonasaki E, Zobra T, Papadopoulou L, Pavlidou E, Chatzistavrou X, Paraskevopoulos K, Koidis P. (2002) Hydroxy Carbonate Apatite Formation on Particulate Bioglass In Vitro as a Function of Time. J Cryst Res Technol 2002; 37:1165–71. DOI:10.1002/1521-4079(200211)37:11<1165::AID-CRAT1165>3.0.CO;2-R

Liu X, Ding C, Chu PK. (2004) Mechanism of apatite formation on wollastonite coatings in simulated body fluids. Biomaterials 2004; 25(10):1755–61. DOI: 10.1016/j.biomaterials.2003.08.024.

Maeno S, Niki Y, Matsumoto H, Morioka H, Yatabe T, Funayama A, Toyama Y, Taguchi T, Tanaka J. (2005) The effect of calcium ion concentration on osteoblast viability, proliferation and differentiation in monolayer and 3D culture. Biomaterials 2005;26(23):4847-55 DOI:10.1016/j.biomaterials.2005.01.006

Mezahi FZ, Oudadesse H, Harabi A, Lucas-Girot A. (2012) Effect of ZrO_2, TiO_2 and Al_2O_3 additions on process and kinetics of bonelike apatite formation on sintered natural hydroxyapatite surfaces. International Journal of Applied Ceramic Technology 2012;9(3):529-40. DOI: 10.1111/j.1744-7402.2011.02742.x.

Mezahi FZ, Oudadesse H, Harabi A, Lucas-Girot A., Le Gal Y, Chaair H, Cathelineau G. (2009) Dissolution kinetic and structural behaviour of natural hydroxyapatite vs. thermal treatment. Journal of Thermal Analysis and Calorimetry 2009; 95:21-9. DOI: 10.1007/s10973-008-9065-4.

Ming W, Ruzhong Z, Weiqing M, Yi L. (2011) Sol–gel derived CaO–SiO2–P2O5 glass/CaSiO3 ceramic composites: processing and electrical properties. J Mater Sci Mater Electron 2011;22: 843–8. DOI: 10.1007/s10854-010-0223-7.

Nabiyouni M, Brückner T, Zhou H, Gbureck U, Bhaduri SB. (2018) Magnesium-based bioceramics in orthopedic applications. Acta biomaterialia 2018; 66:23-43 DOI: 10.1016/j.actbio.2017.11.033.

Nonami T, Tsutsumi S. (1999) Study of diopside ceramics for biomaterials. J. Mater. Sci Mater Med 1999;10(8):475-9. DOI: 10.1023/a:1008996908797.

Nonami T. (1992) Developmental study of diopside for use as implant material. Mater Res Soc Proc 1992; 252:87–92. DOI: 10.1557/PROC-252-87.

Omori K. (1971) Analysis of the infrared absorption spectrum of diopside. Am Mineral 1971; 56:1607–16. [Google Scholar].

Palakurthy S, Abdul Azeem P, Venugopal Reddy K, Padala Ch, Bramanandam M, Rao RP. (2021) A novel cost-effective approach to fabricate diopside bioceramics: A promising ceramics for orthopedic applications. Adv Powder Technol 2021;32(3):875-84. DOI:10.1016/j.apt.2021.01.038.

Python M, Ishida Y, Ceuleneer G, Arai S. (2007) Trace element heterogeneity in hydrothermal diopside: Evidence for Ti depletion and Sr-Eu-LREE enrichment during hydrothermal metamorphism of mantle harzburgite. J Mineral Petrol Sci 2007;102(2):143–9. DOI: 10.2465/jmps.060830.

Sadeghzade S, Emadi R, Tavangarian F, (2017) Naderi M. Fabrication and evaluation of silica-based ceramic scaffolds for hard tissue engineering applications. Mater Sci Eng: C 2017; 71:431–8. doi.org/10.1016/j.msec.2016.10.042.

Saravanan C, Sasikumar S. (2012) Bioactive diopside ($CaMgSi_2O_6$) as a drug delivery carrier a review. Current Drug Delivery 2012; 9:583–7. DOI: 10.2174/156720112803529765

Shahrouzifara MR, Salahinejada E, Sharifib E. (2019) Co-incorporation of strontium and fluorine into diopside scaffolds: Bioactivity, biodegradation and cytocompatibility evaluations. Mater Sci Eng C 2019; 103:1-9. DOI: 10.1016/j.msec.2019.109752.

Shen J, Yang X, Wu R, Shen M, Lu F, Zhang F, Chen Z, Chen X, Xu S, Gao C. (2020) Direct ink writing core-shell Wollastonite @ Diopside scaffolds with tailorable shell micropores favorable for optimizing physicochemical and biodegradation properties. J. Eur Ceram Soc 2015; 40(2):503-12. doi.org/10.1016/j.jeurceramsoc.2019.09.049.

Sobhani A, Salimi E. (2023). Low temperature preparation of diopside nanoparticles: in‑vitro bioactivity and drug loading evaluation 2023;13:11. DOI: 10.1038/s41598-023-43671-0.

Titorenkova R, Kostov-Kytin V, Dimitrov T. (2022) Synthesis, phase composition and characterization of Co-diopside ceramic pigments. Ceram Int 2022;48(24):36781–8. doi.org/10.1016/j.ceramint.2022.08.242.

Vallet-Regi V, Salinas A J, Roman J, Gil M. (1999) Effect of magnesium content on the in vitro bioactivity of CaO–MgO–SiO2–P_2O_5 sol–gel glasses. J Mater Chem 1999;9:515–8. DOI: 10.1039/a808679f.

Venkatraman S K, Choudhary R, Krishnamurithy G, Raghavendran HRB, Murali MR, Kamarul T, Suresh A, Abraham J, Praharaj S, Swamiappan S. (2022) Comparative investigation on antibacterial, biological and mechanical behaviour of monticellite and diopside derived from biowaste

for bone regeneration. Mater Chem and Phys 2022;286:126-57. doi.org/10.1016/j.matchemphys.2022.126157.

Venkatraman SK, Swamiappan S. (2020) Review on calcium-and magnesium-based silicates for bone tissue engineering applications. J. Biomed Mater Res A 2015;108(7):1546-62. doi.org/10.1002/jbm.a.36925.

Wu C, Chang J. (2007) Degradation, bioactivity, and cytocompatibility of diopside, akermanite, and bredigite ceramics. J Biomed Mater Res 2007;83B:153–60. DOI: 10.1002/jbm.b.30779.

Yamamoto S, Kawamura N, Nonami T. (2019) Diopside synthesized by sol-gel method as phosphorus adsorption material: Evaluation of apatite deposition in pseudo body solution. Trans Mater Res Soc Jpn 2019;44(1):17–23. doi.org/10.14723/tmrsj.44.17.

Yoshizawa S, Brown A, Barchowsky A, Sfeir C. (2014) Magnesium ion stimulation of bone marrow stromal cells enhances osteogenic activity, simulating the effect of magnesium alloy degradation. Acta biomaterialia 2014;10(6):2834-42. DOI: 10.1016/j.actbio.2014.02.002

Zhu H, Guo D, Zang H, Hanaor DA, Yu S, Schmidt F, Xu K. (2020) Enhancement of hydroxyapatite dissolution through structure modification by Krypton ion irradiation. J Mater Sci Technol 2015; 38:148-58. doi.org/10.1016/j.jmst.2019.03.048.